

# Chapter 18

## Microstructure and Mechanical Properties of IN738C Superalloy Fabricated by Laser Powder Bed Fusion



Han Zhang, Quanquan Han, Zhongyi Liu, Zhenhua Zhang, Zhongyang Sui, and Liqiao Wang

**Abstract** IN738C is a widely utilized precipitation hardening nickel-based superalloy known for its excellent mechanical properties in various industries. Laser powder bed fusion (LPBF) has emerged as a highly advantageous additive manufacturing process for fabricating complex-shaped parts using metal powders. This study investigates the influence of process parameters, specifically the scanning speed and hatch spacing, on the defect formation in LPBF-manufactured IN738C alloy. Additionally, the microstructure of heat-treated IN738C samples is examined, and their mechanical properties are evaluated through ambient tensile testing. The results indicate that LPBF-produced IN738C alloy exhibits the highest density when using a hatch spacing of 90  $\mu\text{m}$  and a scanning speed of 750 mm/s. Upon heat treatment, cracks within the material propagated. Microscopic analysis of the heat-treated specimens reveals the presence of precipitated carbides and the  $\text{O3B3}'$  phase, with continuous carbides observed along the grain boundaries. The as-built (AB) specimens exhibit a medium result in ultimate tensile strength (UTS), yield strength (YS), and elongation. However, the heat-treated (HT) specimens fail prior to yielding, exhibiting a lower result in UTS and elongation than AB specimens.

### 18.1 Introduction

Nickel-based superalloys are extensively employed in applications that demand excellent mechanical properties at high temperatures, particularly within the aerospace industry. As operating temperatures continue to increase, the significance of precipitation hardening nickel-based superalloys becomes more pronounced across various sectors. IN738C, also known as Inconel 738C, represents a typical

---

H. Zhang · Q. Han (✉) · Z. Liu · Z. Zhang · Z. Sui · L. Wang  
Key Laboratory of High Efficiency and Clean Mechanical Manufacture of Ministry of Education, School of Mechanical Engineering, Shandong University, Jinan 250061, China  
e-mail: [hanquanquan@sdu.edu.cn](mailto:hanquanquan@sdu.edu.cn)

example of a precipitation hardening nickel-based superalloy. Due to its exceptional high-temperature performance and corrosion resistance, it has found widespread use in critical components such as the hot sections of gas turbine and jet engines, as well as nuclear reactor parts [1, 2].

The complexity of part geometries has grown, posing challenges for traditional machining methods in processing superalloys. Additive Manufacturing (AM), a novel fabrication technique, offers an alternative approach. Unlike conventional methods, AM constructs parts layer by layer, starting from scratch. By employing thinner layers and precise control of the scanning path, AM enables the production of parts with minimal dimensional errors. Theoretically, AM has the capability to manufacture parts with highly intricate geometries [3]. One specific AM technology is laser powder bed fusion (LPBF), which utilizes metal powder as the raw material. Through a cyclic process involving powder deposition and laser scanning, LPBF can fabricate parts which need little machining based on a computer-aided design (CAD) model. Compared with other manufacturing process, this feature allows LPBF to conserve energy and materials, making it a sustainable manufacturing process. At present, however, there are still some problems in LPBF-fabricated parts, which may lead to significant failures, causing a waste of materials. It has a great significance to sustainable manufacturing in research of the present problems.

In recent years, significant research efforts have been devoted to exploring the fabrication of nickel-based superalloys using LPBF. Ma et al. [4] reported that liquation cracks were the primary defect observed in LPBF-fabricated IN738 alloy [4]. The influence of scanning strategies [5, 6] and heat treatment methods [7] on the crack density of IN738 alloy has been investigated. It has been established that selecting appropriate process parameters can reduce crack density; however, completely eliminating cracks remains a challenge [5–7]. The present study aims to investigate the impact of hatch spacing and scanning speed on the occurrence of defects in LPBF-fabricated IN738C. Additionally, the cracking mode of IN738 alloy is examined. Subsequently, the microstructure of IN738 is studied following heat treatment, and a tensile test is conducted to assess the effect of heat treatment on the mechanical properties of the specimens.

## 18.2 Experimental Procedure

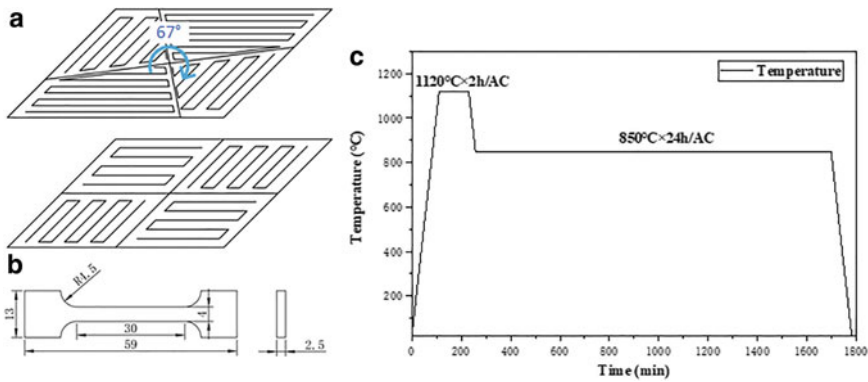
### 18.2.1 Material and Manufacturing Processes

The feedstock of IN738C (Avimetal AM) used in this study was produced through vacuum atomization. The composition of the IN738C powder is provided in Table 18.1. The particle size distribution of the powder, characterized by the D10, D50, and D90 values, is detected to 19.1  $\mu\text{m}$ , 33.3  $\mu\text{m}$ , and 55.1  $\mu\text{m}$ , respectively.

All specimens in this study were manufactured on 45-steel substrates, using a Concept Laser Mlab cusing 200R laser powder bed fusion (LPBF) machine under an

**Table 18.1** Actual chemical composition of the IN738 powder

Element	Cr	Co	W	Mo	Al	Ti	Nb	Ta	C	Ni
wt. %	15.92	8.12	2.61	1.8	3.6	3.49	0.94	1.78	0.17	Bal

**Fig. 18.1** Specimen **a** scanning strategy, **b** heat treatment strategy, and **c** tensile bar

argon atmosphere. The LPBF machine was equipped with a 200W ytterbium fiber laser operating at a wavelength of 1070 nm. The laser had a Gaussian spot size of approximately 70  $\mu\text{m}$ .

To optimize the scanning speed and hatch spacing, two groups of cubic specimens measuring  $7 \times 7 \times 8$  mm were initially fabricated. These groups were divided based on different hatch spacings, namely 90 and 110  $\mu\text{m}$ . The main process parameters were kept constant during this optimization process. The laser power used was set at 190 W, and the layer thickness was maintained at 40  $\mu\text{m}$ . The scanning strategy employed was a chessboard pattern, with each island having a side length of 5 mm. In each layer, the scanning direction was rotated by  $90^\circ$ , while the chessboard pattern was rotated by  $67^\circ$ , as depicted in Fig. 18.1a.

Tensile test specimens, in the form of panels measuring  $2.5 \times 65 \times 14$  mm, were subsequently manufactured using the optimized parameters obtained from the cubic specimens. The optimal parameters consisted of a hatch spacing of 90  $\mu\text{m}$  and a scanning speed of 750 mm/s. Alongside the tensile specimens, cubic specimens were also fabricated to facilitate microstructure observations.

Heat treatment was conducted using a tubular furnace under an argon atmosphere. The heat treatment strategy employed in this study is illustrated in Fig. 18.1b. It consisted of a solution treatment carried out at 1120  $^\circ\text{C}$  for 2 h, followed by an aging treatment at 850  $^\circ\text{C}$  for 24 h. To ensure the desired treatment conditions, the specimens were placed into the furnace once the temperature reached the prescribed treatment temperature. After each heat treatment stage, the specimens were air-cooled (AC) to ambient temperature.

### 18.2.2 *Microstructure Observation*

The cubic specimens were cut using wire cutting parallel to the build direction. The cut sections were then ground sequentially using SiC sandpaper with grit sizes of 320, 600, 1500, and 2500 mesh. Following the grinding process, the samples were polished using polishing suspensions of 3, 1, and 0.04  $\mu\text{m}$ .

The polished specimens were initially examined using an optical metallographic microscope to evaluate the presence of defects such as lack of fusion, microcracks, and keyholes. The optimization of LPBF parameters was performed under the optical observation with a magnification of 50 times. The parameters of cubic specimen with less lack of fusion and keyhole defects were selected to be optimal. Also, 5 areas were observed and averaged for each specimen in the optimization. For microstructure observation, scanning electron microscopy (SEM) was utilized, specifically the JEOL JSM-7800F model. To further analyze the microstructures, the specimens were etched in a 15% oxalic acid solution using a 5 V direct current. Energy-dispersive X-ray spectroscopy (EDS) equipped on the Zeiss Gemini500 SEM was employed to analyze the micro-segregation of elements within specific regions of interest.

To determine the average diameters of carbides and  $\gamma'$  phase, the 'Analyze particles' function in the ImageJ software was utilized. The measurements were subsequently calculated using Excel. In order to ensure data reliability, any unreasonable data points, such as particles with only a few pixels, were manually excluded from the analysis.

A single path LPBF simulation was carried out by the Flow3D software to understand the mechanism of the cracks observed in LPBF-fabricated IN738C. The parameters used in the simulation were set according to the optimized LPBF process parameters and physical properties of IN738 superalloy.

The JMatPro software was utilized in the equilibrium thermodynamic simulation of IN738 used in the experiment. The simulation was carried out over a temperature range from 1400 to 600  $^{\circ}\text{C}$ , with a step of 1  $^{\circ}\text{C}$ . The simulation output includes the weight fractions of the various phases at each temperature steps.

### 18.2.3 *Tensile Test*

The tensile specimens were fabricated as panels, using the optimized parameters obtained from the previous fabrication process. Subsequently, half of the panels underwent a standard heat treatment same as mentioned in Sect. 2.1, which consisted of a solution treatment at 1120  $^{\circ}\text{C}$  for 2 h, followed by an aging treatment at 850  $^{\circ}\text{C}$  for 24 h, with air cooling (AC) after each stage.

Plate tensile bars, both as-built (AB) and heat-treated (HT), were obtained by wire cutting from the panels, ensuring that the load direction was perpendicular to the build direction. The dimensions of the tensile specimens, designed according to the GB/T 228.1-2021 standard, are illustrated in Fig. 18.1c.

The tensile tests were performed using a universal testing machine, applying a constant strain rate of  $0.067 \text{ min}^{-1}$  at ambient temperature. To minimize errors, two specimens from both the AB and HT groups were tested.

## 18.3 Results and Discussion

### 18.3.1 *Characterization of Defects in LPBF-Fabricated IN738C*

The polished specimens were examined using an optical metallographic microscope. Keyholes were only observed in specimens fabricated at low scanning speeds, whereas lack of fusion was observed in specimens fabricated at high scanning speeds. Microcracks were observed in all specimens, regardless of scanning speed.

Notably, specimens fabricated at medium scanning speeds exhibited a lower cracking density compared to those at other scanning speeds, regardless of the hatch spacing (90 and 110  $\mu\text{m}$ ). Among the specimens in the 90  $\mu\text{m}$  group, a lower cracking tendency was observed compared to the 110  $\mu\text{m}$  group across all scanning speeds. Specifically, the specimen fabricated at a scanning speed of 750 mm/s in the 90  $\mu\text{m}$  group exhibited the lowest cracking tendency among all specimens, characterized by a lower cracking density and smaller microcracks.

In contrast to previous research [4], the present study identified two primary types of microcracks in LPBF-fabricated IN738C: solidification cracks and solid-state cracks, as depicted in Fig. 18.2a. Solidification cracks are characterized by their width and winding patterns, which are often aligned horizontally to the build direction. Figure 18.2b illustrates a typical example of a solidification crack, with the winding portion situated in the middle. Upon closer examination, dendrite arms were observable within the crack structure. On the other hand, solid-state cracks tend to be thinner, straighter, and exhibit a small winding tail at the end. Moreover, solid-state cracks display symmetrical edges, which is not the case for solidification cracks. Within LPBF-fabricated IN738C specimens, approximately half of the observed cracks are solidification cracks, while the remaining half are solid-state cracks. Notably, the length and density of the cracks exhibit significant variation, both within specimens fabricated using the same parameters and among those fabricated using different parameters. The minimum crack length and density were achieved when employing a hatch spacing of 90  $\mu\text{m}$  and a scanning speed of 750 mm/s.

The cracking density in LPBF-fabricated specimens exhibited significant variation depending on the selected process parameters. Specifically, the cracking density demonstrated an initial decrease followed by an increase with increasing scanning speed, while the hatch spacing remained constant. Moreover, the type of defects observed varied with changes in scanning speed, transitioning from a combination of keyhole defects and cracking, to solely cracking, and eventually to lack of fusion

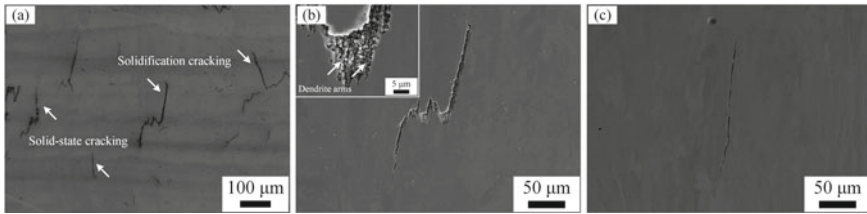


**Fig. 18.2** Backscattered electron imaging SEM micrographs of microcracks in as-built LPBF-fabricated IN738 specimen **a** overview, **b** solidification cracking, and **c** solid-state cracking

and cracking as the speed rises. These changes in defect type can be attributed to alterations in energy density among the specimens.

At lower energy densities, the metal powders may not fully melt, resulting in the occurrence of lack of fusion defects. Conversely, higher energy densities can lead to excessive heating, resulting in the formation of keyhole defects where the fused metal boils and creates voids. Cracking defects can arise due to inadequate bonding strength resulting from lower energy densities, while higher energy densities can contribute to greater residual stress, increasing the likelihood of cracking. The lowest cracking density appeared at a  $70.37 \text{ J/mm}^3$  volume energy density, which is included in  $64.9\text{--}118.6 \text{ J/mm}^3$  in the previous research [5]. These factors related to energy density are considered to be the main driving force behind the observed variations in cracking density.

In LPBF-fabricated specimens, two distinct types of cracks were observed: solidification cracks and solid-state cracks. Figure 18.3 provides an illustration of the three main zones present during the scanning process: the melt pool, the transition zone, and the heat-affected zone. Solidification cracks predominantly manifested at the boundary between the melt pool and the transition zone. During the solidification process, the unsolidified liquid film situated between the dendrites became unable to withstand the tensile stress, resulting in the formation of solidification cracks. These cracks were characterized by the presence of dendrite arms, indicative of their occurrence during the solidification phase.

On the other hand, solid-state cracks primarily appeared in the heat-affected zone. The LPBF process subjected the specimens to a thermal cycle, inducing thermal stress within the heat-affected zone. Solid-state cracks formed when the thermal stress exceeded the material's limit of resistance. These cracks exhibited symmetrical edges and typically had a sharp, winding termination, suggesting they were formed through tearing after the solidification stage.

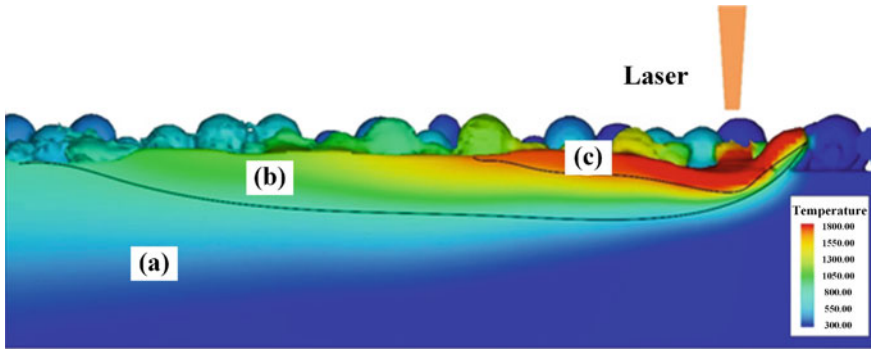


**Fig. 18.3** Three zones existed in LPBF process **a** heat-affected zone, **b** transition zone, and **c** the melt pool

### 18.3.2 Characterization of Heat-Treated IN738C

In comparison to the as-built specimens, the heat-treated specimens exhibited longer and wider solid-state cracks. Figure 18.4 illustrates the morphology of the solid-state cracks, which appeared elongated and wider, while the solidification cracks seemed to be stretched, displaying a longer edge compared to the cracks observed in the as-built specimens. During the LPBF process, significant thermal stress is generated, some of which is relieved through cracking, while the remaining stress is retained within the fabricated specimens. This retained stress can be released through recrystallization or by cracking during the heat treatment process, thereby elongating the existing cracks present in the specimens. According to a previous study carried out by Zhang et al [8], the microcracks generally occurred on the grain boundaries.

The etched specimens were examined using SEM, and the results are presented in Fig. 18.5a. The grains exhibited a columnar morphology, with dark lines observed at the grain boundaries. Figure 18.5b provides a micrograph of the grain boundaries,

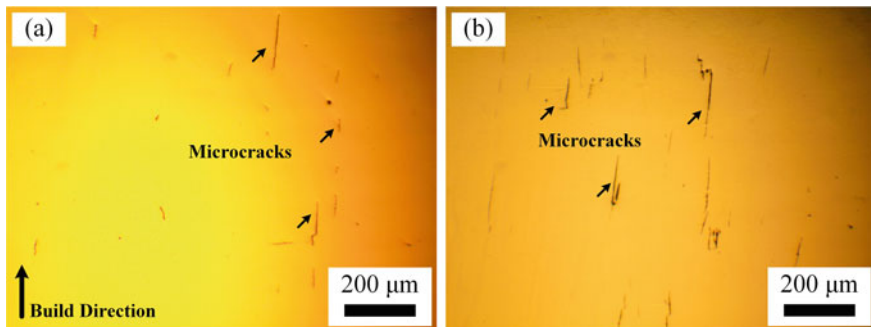


**Fig. 18.4** Optical micrographs of **a** as-built specimen, and **b** heat-treated specimen under same LPBF process parameters

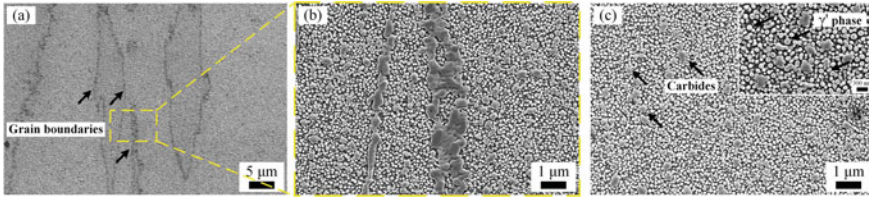


**Fig. 18.5** Secondary electron (SE) imaging SEM micrographs of heat-treated specimens **a** overview, **b** micrograph near grain boundaries, and **c** micrograph in a grain

where irregularly shaped dark precipitates were found continuously aligned along the grain boundaries. EDS mapping analysis revealed a deficiency of Ni, Co, and Al at the location of the precipitates, while an accumulation of Ta, W, Cr, Nb, and C was observed at the same position, as shown in Fig. 18.6. This observation suggests the precipitation of carbides at the grain boundaries following the heat treatment. Based on the concentrated elements detected in the precipitates, it can be inferred that the carbides consist of MC and M<sub>23</sub>C<sub>6</sub> phases. Equilibrium thermodynamic simulations of IN738C indicate that at high temperatures, the carbides primarily exist as MC. However, at approximately 1093 °C, the MC carbides begin to transform into M<sub>23</sub>C<sub>6</sub> carbides. At around 981 °C, the M<sub>23</sub>C<sub>6</sub> carbides become the sole type of carbide present in the IN738C superalloy. The observed mixture of MC and M<sub>23</sub>C<sub>6</sub> carbides suggests that the carbide transformation in the LPBF-fabricated specimens was not fully completed under typical heat treatment conditions.

In Fig. 18.5c, a micrograph inside a grain is shown. Irregularly shaped carbides were observed to be dispersed evenly throughout the matrix, with an average diameter of 309.5 nm. Additionally, small spherical precipitates with an average diameter of 159.2 nm were uniformly distributed within the matrix. These observations indicate the precipitation of the  $\gamma'$  phase ([Ni<sub>3</sub>(Al, Ti)]). The  $\gamma'$  phase is a crucial strengthening phase in precipitation hardening nickel-based superalloys, particularly at high temperatures. The morphology of the  $\gamma'$  phase can vary and may appear as spherical, irregular, or cubic shapes depending on the diameter of the precipitates. Generally, the presence of spherical  $\gamma'$  phase morphology corresponds to excellent mechanical properties. The observation of spherical  $\gamma'$  phase indicates that the heat treatment regimen employed in this study was appropriate. Together with the precipitation of carbides, the uniform precipitation of the  $\gamma'$  phase contributes to the strengthening of the IN738C alloy [9].

### 18.3.3 Ambient Temperature Tensile Test

The results of the ambient temperature tensile tests for both as-built (AB) and heat-treated (HT) IN738C specimens are presented in Fig. 18.7. The AB specimens exhibited an ultimate tensile strength (UTS) of  $811.6 \pm 4.7$  MPa, a yield strength (YS) of



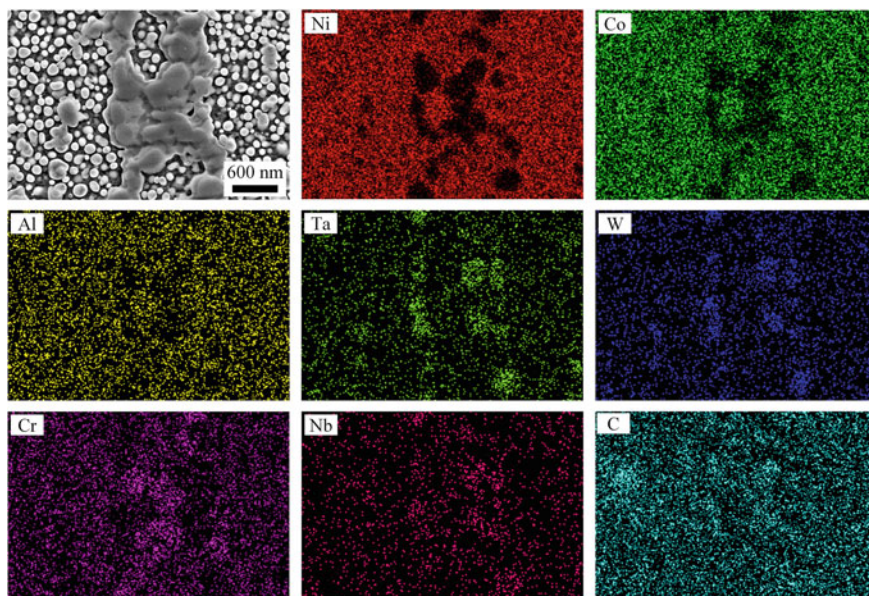


**Fig. 18.6** Energy-dispersive X-ray spectroscopy (EDS) mapping of the precipitates on the grain boundaries in heat-treated specimens

600.8 ± 6.1 MPa, and an elongation of 10.35 ± 0.17%. In contrast, the HT specimens experienced failure before yielding, with a UTS of 673.4 ± 18.45 MPa and an elongation of 4.21 ± 0.06%. The UTS of AB specimens was lower than the value reported in previous study, while elongation was much higher. The HT specimens got both a lower UTS and elongation [5].

The low tensile properties of the AB IN738C specimens can be attributed to the presence of microcracks within the specimens. These microcracks can serve as stress concentrators and become the initiation points for failure during the tensile testing. Additionally, the presence of microcracks reduces the effective area available to withstand tensile stress, further contributing to the poor performance of the AB specimens.

Although the heat treatment resulted in the precipitation of strengthening phases, the HT specimens exhibited worse tensile properties compared to the AB specimens. This can be attributed to the more severe cracking observed in the HT specimens, which led to failure occurring earlier before the specimens could yield.

Overall, the presence of microcracks in the AB specimens and the increased cracking in the HT specimens negatively impacted their tensile properties, resulting in reduced strength and elongation compared to the desired performance.

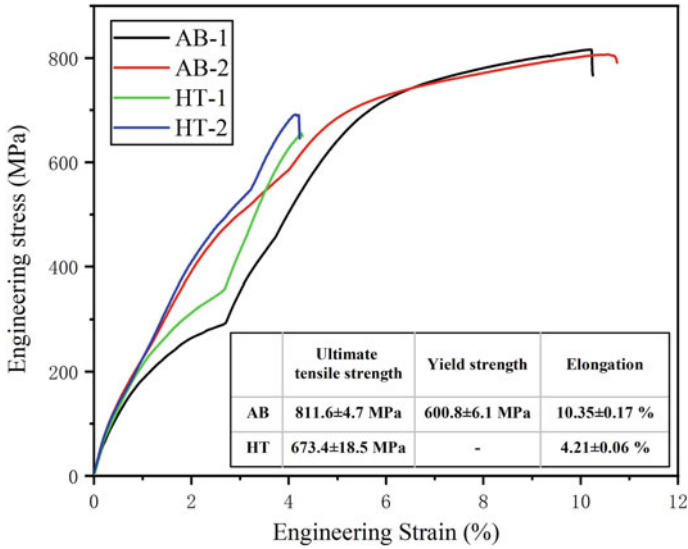


Fig. 18.7 Ambient temperature tensile test

### 18.4 Conclusion

This study optimized the hatch spacing and scanning speed of IN738C in LPBF processing. The main findings of the study can be summarized as follows:

- (1) Different types of defects were observed in LPBF-fabricated IN738C, including lack of fusion, cracking, and keyhole. It was found that a parameter combination with relatively lower cracking density could be achieved. Lack of fusion and keyhole defects could be eliminated with appropriate process parameters, but cracking could not be completely eliminated even with parameter optimization. The lowest cracking density was observed when the hatch spacing was 90 μm and the scanning speed was 750 mm/s. After heat treatment, cracks in the specimens elongated.
- (2) SEM observations of the heat-treated specimens revealed the presence of continuous carbides at the grain boundaries. EDS mapping indicated the concentration of Ta, W, Cr, Nb, and C, suggesting the presence of MC carbides and M23C6 carbides. Smaller carbides were also observed inside the grains, with an average diameter of 309.5 nm. Additionally, spherical γ' phase with an average diameter of 159.2 nm uniformly precipitated in the matrix after heat treatment.
- (3) The tensile test of the as-built specimens at ambient temperature showed an ultimate tensile strength (UTS) of 811.6 ± 4.7 MPa, a yield strength (YS) of 600.8 ± 6.1 MPa, and an elongation of 10.35 ± 0.17%. However, the heat-treated specimens failed before yielding, with a lower UTS of 673.4 ± 18.45 MPa and

a reduced elongation of  $4.21 \pm 0.06\%$ . The decrease in mechanical properties was mainly attributed to the increase of the microcracks.

Overall, the study highlighted the challenges of eliminating cracking in LPBF-fabricated IN738C, the presence of carbides and  $\gamma'$  phase after heat treatment, and the impact of heat treatment on the mechanical properties of the alloy.

## References

1. Mouritz, A.P.: Superalloys for Gas Turbine Engines, Introduction to Aerospace Materials, pp. 251–267 (2012)
2. Perrut, M., Caron, P., Thomas, M., Couret, A.: High temperature materials for aerospace applications: Ni-based superalloys and  $\gamma$ -TiAl alloys. *Compt. Rendus Phys.* **19**(8), 657–671 (2018)
3. Han, Q., Gu, H., Soe, S., Setchi, R., Lacan, F., Hill, J.: Manufacturability of AlSi10Mg overhang structures fabricated by laser powder bed fusion. *Mater. Des.* **160**, 1080–1095 (2018)
4. Ma, Y., Xu, J., Gao, Y., Liu, B., Hu, Y., Ding, Y., Chen, D., Chen, H.: Evolution and formation mechanism of defect in SLM-built inconel 738 alloy. *Mater. Rep.* **36**(13), 166–172 (2022)
5. Yan, H., Zhu, G., Shi, H., Zhang, P., Li, H., Lu, Q., Li, Z.: Microstructure and mechanical properties of K438 alloy processed by selective laser melting and subsequent heat treatment. *Mater. Charact.* **191**, 112116 (2022)
6. Guo, C., Zhou, Y., Li, X., Hu, X., Xu, Z., Dong, E., Zhu, Q., Ward, R.: A comparing study of defect generation in IN738LC superalloy fabricated by laser powder bed fusion: continuous-wave mode versus pulsed-wave mode. *J. Mater. Sci. Technol.* **90**, 45–57 (2021)
7. Xu, J., Ding, Y., Gao, Y., Wang, H., Hu, Y., Zhang, D.: Grain refinement and crack inhibition of hard-to-weld Inconel 738 alloy by altering the scanning strategy during selective laser melting. *Mater. Des.* **209**, 109940 (2021)
8. Zhang, Z., Han, Q., Liu, Z., Wang, X., Wang, L., Yang, X., Ma, T., Gao, Z.: Influence of the TiB<sub>2</sub> content on the processability, microstructure and high-temperature tensile performance of a Ni-based superalloy by laser powder bed fusion. *J. Alloy. Compd.* **908**, 164656 (2022)
9. Zhou, W., Tian, Y., Tan, Q., Qiao, S., Luo, H., Zhu, G., Shu, D., Sun, B.: Effect of carbon content on the microstructure, tensile properties and cracking susceptibility of IN738 superalloy processed by laser powder bed fusion. *Addit. Manuf.* **58**, 103016 (2022)